COMPUTATIONAL INVESTIGATION OF THE EFFECTS OF SPHERICAL FILLER MORPHOLOGY AND LOADING ON DIFFUSION TORTUOSITY AND RUBBER PERMEABILITY

T. C. GRUBER,* S. D. CROSSLEY, A. P. SMITH
TECHNOLOGY LABORATORY, BIRLA CARBON, MARIETTA, GA 30062

RUBBER CHEMISTRY AND TECHNOLOGY, Vol. 86, No. 2, pp. 175–189 (2013)

ABSTRACT

Inflation pressure loss in tires degrades performance, raises rolling resistance, and reduces fuel economy. The incorporation of solid fillers, such as carbon black, at relatively high loadings in tire innerliners helps minimize these pressure losses by reducing innerliner permeability due to increases in average gas molecule diffusion path lengths (tortuosity), as well as reductions in diffusion pathway density (capacity). The effects of filler morphology and loading on diffusion path tortuosity can be explored by modeling biased random-walk diffusion through impermeable sphere-filled matrices. Modeled diffusion rate was found to decrease with increased filler loading, reduced filler sphere sizes, increased random-walk step sizes, and the aggregation of filler spheres. Initial correlations with limited empirical permeability measurements are used to validate the model approach.
[doi:10.5254/rct.13.88932]

INTRODUCTION

Carbon black morphology and loading have wide-ranging effects on rubber composite properties, including tensile strength, modulus, tear and wear resistance, thermal and electrical conductivity, loss modulus/heat buildup, coefficient of friction, and UV degradation resistance, among many others.[1] In some cases, carbon black morphology is chosen to optimize a few key compound properties and to merely fall within acceptable ranges in other properties. In the historical use of carbon black in tire innerliner compounds, reduced permeability may have been simply an ancillary benefit of reducing the cost by increasing filler loading where possible. Innerliner permeability can be reduced by changing or modifying polymers or additives rather than optimizing carbon black type and loading, but the increasing importance of maximizing fuel economy concomitantly mandates optimizing all aspects of pneumatic tire gas retention. Reductions in permeability also allow thinning the innerliner layer, which produces energy savings by reducing a tire's moment of inertia. Rubber permeability measurements, although obviously indispensable, are costly, time consuming, and experimentally challenging and, therefore, not well-suited for combinatorial screening of large regions of the hyperdimensional innerliner compound sample space. The present study is envisioned to help fill this need by providing a computational means of exploring the effects of filler morphology on rubber compound permeability and thereby providing guidance to the process of engineering rubber composites.

Since its invention in 1937, butyl rubber has often been used in gas retention applications (for example, tire innerliners) because of its low permeability. Later, other rubbers having even lower permeability (e.g., halobutyls, such as bromobutyl) were developed and used. Besides polymer type, the barrier effects of fillers are also very important, and although a complete review is not intended here, a few examples indicate the historical interest in this area. In studying the effects of various carbon blacks on natural rubber permeability in 1955, van Amerongen[2] reported that the permeability of rubber was reduced about 30% by adding 50 phr of different types of carbon black across a significant range of carbon black morphology space (structure and surface area). The data

*Corresponding author. Email: tyler.gruber@adityabirla.com

indicated only small differences in permeability decreases between carbon black grades, with higher surface area grades imparting slightly greater decreases. van Amerongen[2] found that, as carbon black fineness increased, the solubility of gas in rubber increased, but the rate of diffusion of the gas decreased, leading to relatively constant permeability at different levels of fineness. These effects were attributed to the adsorption of gas by the carbon black surface. A distinction was made between transient and steady-state permeability; the latter is generally important and is the property under consideration in this work. The same author, in a subsequent review of diffusion in elastomers,[3] described the potential contributions of other filler morphologies to permeability properties. Of importance, he noted that the percentage reductions in permeability via incorporations of approximately 0.2 volume loadings of various fillers were fairly similar. These fillers included wide ranges of carbon blacks and a variety of mineral fillers, all of which have aggregated nodular morphologies. The exceptions were lamellar or plate-like structures (mica, clays, and similar materials; see Nah and Kader[4] for a modern treatment of this subject), which yielded much greater permeability decreases at approximately equivalent volume fraction than did their nodular counterparts.

For decades, low-structure, carcass-type furnace carbon blacks have dominated filler usage in innerliner applications because of their economy and wide availability, good processing characteristics, and favorable mechanical and permeability properties at high loadings. These properties allow the tire compounder to reduce the thickness and unit cost of the tire innerliner. Thermal carbon blacks, although not widely available, have also been used in some low-permeability applications. Juengel et al.[5] described the commercial development of very low-surface area furnace-type carbon blacks targeted for innerliner applications. These carbon blacks are very low in structure, are intermediate in fineness between conventional carcass-type and thermal-type carbon blacks, and reportedly yield some advantages for innerliner use at high loadings. The crack growth property enhancements of these materials were also reported in subsequent work (Hardy and Moneypenny et al.[6]) showing low permeability for compounds containing other carbon black types, with filler loadings adjusted to give similar tensile property levels throughout.

Further reports on investigations into solid filler effects on permeability from fundamental and applied points of view have continued, for example, the development in the past few years of lamellar nanocomposite fillers designed to have preferred orientations to minimize compound permeability in one direction (examples include those described in Rodgers et al.[7] and Lohse[8]).

One of the key implications of the behavior observed by van Amorengen and others is that carbon black/filler and polymer contributions to reductions in permeability tend to be relatively decoupled; that is, modification of either portion of the composite often does not significantly affect the (mostly independent) permeability contribution of the other component. The current study makes use of this decoupled behavior by modeling the effects of filler morphology and loading on increases in average diffusion path lengths (tortuosity) without considering the permeability properties of a particular polymer phase. Because permeability depends on both the path length (tortuosity) experienced by diffusing gas molecules and the diffusion capacity of the filled rubber volume, the combined effects of modeled tortuosity and calculated capacity are used to develop an estimate of modeled rubber permeability decrease, which is compared with limited empirical permeability measurements.

EXPERIMENTAL

PERMEABILITY MEASUREMENTS

Two compounds were tested for permeability for comparison with modeling results. N660 was mixed in a model bromobutyl innerliner compound at 100 phr, and testing of cured-unfilled and

TABLE I
MODELING PARAMETER SPACE—CORE STUDY

Parameter	Values	No. of values
Aggregation/sphere overlap	yes, no	2
Mean sphere size, nm	30, 50, 70, 100, 150, 200, 300, 500	8
SS heterogeneity index	1.5, 2.5	2
Sphere loading, phr	20, 40, 60, 80, 100	5
Random-walk step size, nm	1, 2, 5, 10, 20	5

100-phr–filled compounds was conducted by ARTIS (Melksham, Wiltshire, U.K.) according to ISO 2782, manometric method, using N_2 at 23 °C and 4×10^5 Pa (gauge).

TORTUOSITY MODELING

Log-normally distributed spheres having a specified mean sphere size (MSS) and heterogeneity index (HI) were generated and placed randomly in an empty sample volume (matrix) until a specified loading was reached. Matrix and sphere densities were assumed to be 0.93 and 1.86 g/cm^3, respectively. In different studies, aggregation was (1) excluded, by requiring replacement of overlapping spheres; or (2) allowed. The spheroidal nodules (particles) that compose carbon black aggregates are analogous to these spheres. Dimensionless particles were then diffused through the matrix via a three-dimensional (3D) random-walk model of specified step size. The random walk was biased in one direction to simulate a pressure gradient. Particles encountering a sphere surface were reflected. The total number of steps required to traverse a set distance parallel to the bias vector was used to calculate an average decrease in diffusion rate, relative to that in an unfilled matrix, due to path tortuosity.

Twenty different volumes were constructed, and 50 μm of diffusion distance, parallel to the bias vector, was modeled for each volume, yielding a total of 1 mm of modeled diffusion for each parameter set. The core of the computational experiment was a systematic study in which a five-dimensional parameter space (defined in Table I) was probed.

For the experiments in which sphere aggregation was permitted, the degree of aggregation (e.g., the structure level analogous to the oil absorption number [OAN], for carbon black) was not explicitly controlled or measured. In the tests allowing aggregation, higher loading volumes will generally have higher degrees of aggregation (a greater degree of sphere overlap).

Further details of the computations employed in this study are provided in Appendix A.

RESULTS

PERMEABILITY MEASUREMENTS

Permeability testing results are given in Table II. The magnitude of the decrease in permeability with the inclusion of N660 carbon black @ 100 phr was found to be 44%. The data from multiple trials indicate that the reproducibility of the permeability measurements is within a few percentage points.

TORTUOSITY MODELING

For clarity, four of the eight core fineness levels probed were chosen to illustrate the trends of the results in the following discussion. These fineness levels encompass the morphological space

TABLE II
EXPERIMENTAL PERMEABILITY DECREASES AS A PERCENTAGE OF 0 PHR PERMEABILITY FOR N660 CARBON BLACK @ 100 PHR-FILLED MODEL BROMOBUTYL INNERLINER COMPOUND (DATA FROM ARTIS)

Sample	Test	Permeability decrease (relative to mean of 0 phr), %	Mean for sample, %
Bromobutyl + 0 phr N660 CB	1	0.0	0
	2	0.0	
Bromobutyl + 100 phr N660 CB	1	45.3	44
	2	45.5	
	3	40.7	

typically available to the innerliner compound and include MSSs of 30, 70, 150, and 300 nm, which roughly correspond to N330 (tread), N660 (carcass), crossover (between carcass and thermal), and N990 (medium thermal) carbon blacks, respectively. Tables of all results for the core modeling study are given in Appendix B.

The parameter used to describe the computational results is decrease in diffusion rate relative to diffusion through an unfilled matrix. This is an average percentage decrease in progress through the matrix per random-walk step for individual, dimensionless particles modeled as described previously. The decreases can be understood as being caused by increases in diffusion path tortuosity resulting from interactions with filler spheres. This parameter does not consider other permeability-related effects, such as the number of diffusing particles that can be accommodated by the matrix.

Figure 1 shows decrease in diffusion rate as a function of sphere loading in the case of a 5-nm random-walk step size and nonaggregated spheres having a distributional width typical of carbon blacks (HI = 1.5). Modeled diffusion rate exhibits decreases with increased sphere loading over the full range of MSSs studied. Smaller spheres give rise to larger decreases in modeled permeability, but loading has a greater effect. Values for much wider sphere size distributions (HI = 2.5) are shown in Figure 2, and comparison of these data to those in Figure 1 shows minimal differences in the modeled diffusion rates. Sphere size distribution was found to have a weak effect on diffusion rate across the range of parameter space examined (see Appendix B); therefore, the following results focus on typical carbon black distributional width (HI = 1.5) data.

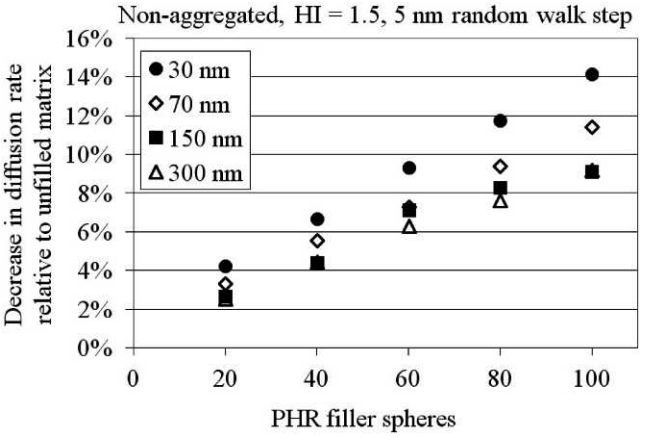

FIG. 1. — Modeled diffusion rate vs phr filler for HI = 1.5, nonaggregated, 5-nm random-walk step.

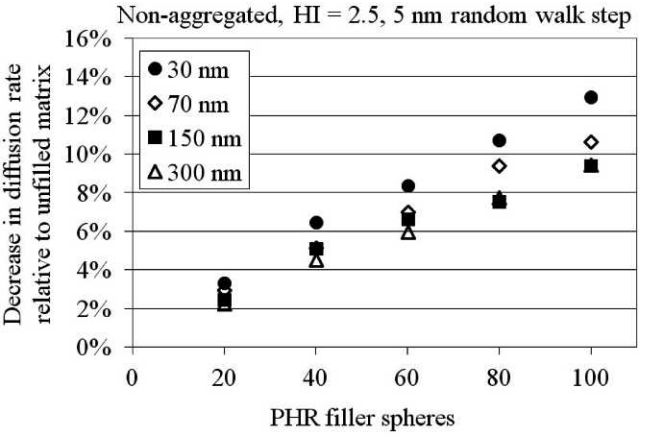

FIG. 2. — Modeled diffusion rate vs phr filler for HI = 2.5, nonaggregated, 5-nm random-walk step.

Next, aggregated filler spheres were investigated. Figure 3 shows the dependence of modeled diffusion rate on loading of aggregated filler spheres. As for the nonaggregated results, diffusion rate decreases with increasing filler loading and with finer fillers. The calculations show that aggregated spheres yield greater decreases in diffusion rate than nonaggregated spheres at a given loading, filler fineness, and random-walk step size.

The random-walk step size of 10 nm was used for Figure 3 because of the unavailability of some data at the 5-nm random-walk step size. It was found that in some of the coarser MSS, higher phr, lower random-walk step size cases, the filler spheres overlapped in such a way as to form "wells" that trapped diffusing particles and stalled their migration. The trapping occurred because the constant bias vector drives particles further into the well until the random-walk vector eventually provides its escape. If the well is deep enough, with respect to the random vector, the particle can remain trapped for a great number of steps before exiting the well and progressing in the direction of the bias vector. This is illustrated in Figure 4, in which the modeled particle enters the well from lower left and escapes at the upper right; dots indicate positions in x and z (y is into the plane) of the diffusing particle at the end of each random-walk step.

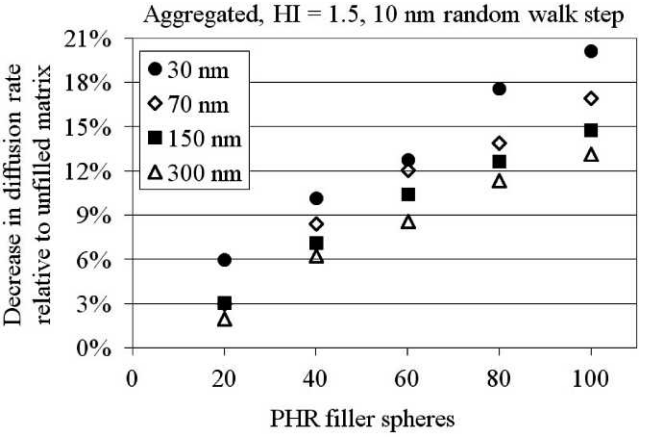

FIG. 3. — Modeled diffusion rate vs phr filler for HI = 1.5, aggregated, 10-nm random-walk step.

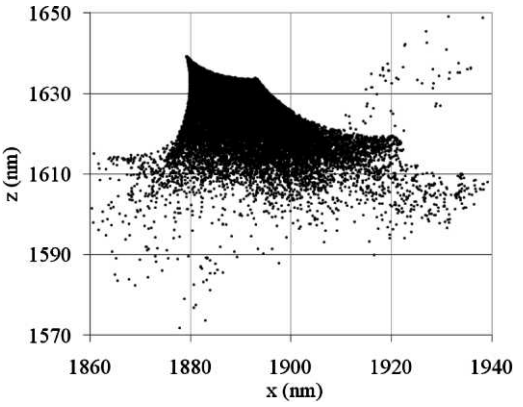

FIG. 4. — Projections on the *x*–*z* plane of a diffusing particle becoming trapped in a "well" formed by aggregated spheres. Length of time to escape the wells depends on the morphology of the well and the size of pressure (bias) and random-walk vectors. MSS = 100 nm, HI = 1.5, 60 phr, random-walk step = 5 nm.

Locations of filler spheres surfaces are evident by the concentration of points visited by the diffusing particle.

In some cases this well-trapping "stalled" the algorithm; although this prevented the tabulation of a few data points at 5-, 10-, and 20-nm random-walk step sizes, it did not detract from establishing the general trends in these data. Because the trapping was more severe for smaller random-walk step sizes, however, it precluded generating meaningful data for the 1- and 2-nm step sizes in the aggregated cases. This behavior has a great impact on the diffusion rate of the biased random walk of a single particle but has limited effect on the overall average diffusion rate of an ensemble of particles moving through a volume.

The random-walk vector step sizes employed in this study are admittedly somewhat arbitrary; a considerable range was tested and compared for each MSS to assess the scope of applicability of the model. Figure 5 shows the results for the aggregated MSS = 30-nm case. Larger random-walk step sizes produce greater decreases in diffusion rate. The trends in the MSS = 30-nm data as a function of random-walk step size are typical of all levels of fineness modeled.

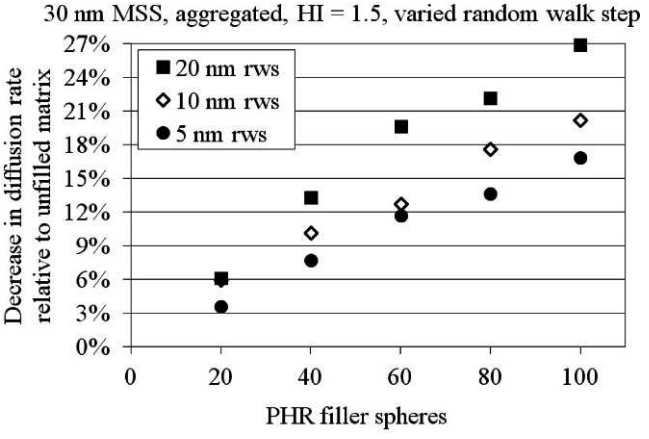

FIG. 5. — Modeled diffusion rate as a function of phr for various random-walk steps (rws). Aggregated, HI = 1.5, MSS = 30 nm.

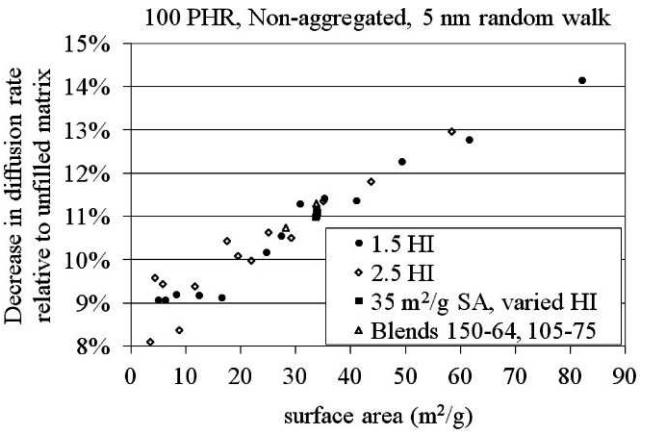

FIG. 6. — Multiple data sets demonstrate the surface area dependence on diffusion-rate decrease for 100 phr individual spheres (5 nm random-walk step).

Variations in all five of the modeled parameters detailed in Table I produced changes in modeled permeability. It was somewhat unexpected that varying the HI from a typical furnace carbon black value (1.5) to a value corresponding to a much broader particle size distribution (2.5) had only an apparently small influence. The influence of morphology was further explored by plotting all 100-phr, 5-nm random-walk step modeled diffusion rates against calculated specific surface areas for nonaggregated sphere distributions (Figure 6). (A typical density value for furnace carbon blacks, 1.86 g/cm^3, was used to calculate mass-specific surface area.) In addition, more atypical distributions were modeled and also included in Figure 6, including log-normal distributions having HI values as small as 1.1 and as large as 8.0, and two 50/50 (by weight), two-component blends of sphere distributions having individual HI values of 1.1 and MSSs of 150/64 nm and 105/75 nm as indicated in the Figure 6 legend. The results indicate that, in this model, surface area alone can account for the changes in modeled diffusion rate, independent of the shape of the sphere size distributions. For a given MSS, therefore, the HI only affects the diffusion rate by modifying the surface area of the filler distribution. The data scatter that increases with lower surface area values in Figure 6 is understood as statistical variability due to sampling considerations; that is, for a given diffusion path length, a diffusing particle interacts with a much smaller number of larger particles in the low surface-area cases.

DISCUSSION

The data in Table II indicate a 44% decrease in experimental permeability in a model bromobutyl innerliner compound with the incorporation of N660 carbon black @ 100 phr. Modeling results tabulated in Appendix B indicate that spheres approximately equivalent to N660-type fineness (MSS = 70 nm, HI = 1.5) @ 100 phr exhibit a modeled diffusion-rate reduction of 9–19% depending on the random-walk step size and the aggregation condition of the model. This apparent discrepancy is understood as follows: Permeability depends not only on the path tortuosity experienced by diffusing gas molecules (the effect of which is modeled and expressed here as diffusion rate) but also on the number of particles that are able to diffuse through the rubber volume at a given instant (capacity), which has not yet been considered. Both effects should have a role in reducing rubber permeability. A first approximation of the permeability suggested by this model, then, would be the product of the diffusion rate (relative to 0 phr) and the concentration of rubber per

unit volume of compound effected by incorporating carbon black (relative to 0 phr). Interpolating and extrapolating the data in Appendix B and giving higher weight to aggregated and smaller step sizes, the predicted tortuosity-induced decrease in diffusion rate for N660-type spheres @ 100 phr is about 13%, corresponding to a relative diffusion rate of 0.87. A carbon black weight loading of 100 phr at the aforementioned assumed densities equates to one-third volume loading, yielding a relative rubber loading (capacity) of two-thirds. The total relative permeability due to both effects (tortuosity and capacity) would then be $0.87 \times (2/3) = 0.58$, corresponding to a permeability decrease of 42%. This agrees well with the experimental permeability reduction (44%) from Table II. Although this singular result lends credence to the modeling approach, further work is clearly needed to verify this relationship and test the modeled diffusion rate and measured permeability results over a broader range of filler loadings and morphologies.

The maximum packing fractions of spheres is known to be most effectively accomplished for a broad size distributions of spheres. In all practical cases for carbon black–filled rubber, the maximum packing fraction of spheres is not approached. For extensively aggregated spheres, the size distributional aspects have less effect than does the aggregate structure on packing considerations. It is realized that the filler morphology and loading properties that might yield optimal permeability characteristics might not be attainable in tire innerliner compounds because of processing requirements and performance considerations and that balancing many properties, of which permeability is only one, is always necessary.

SUMMARY

Biased, random-walk diffusion of particles in volumes filled with nonaggregated and aggregated log-normal sphere distributions has been used to model tortuosity-related diffusion rate in 3D composites of permeable (matrix) and impermeable (spheres) phases. Five parameters were varied, and significant differences were found with parameter values, except for sphere size heterogeneity index. Modeled diffusion rate was reduced with increased loading, sphere fineness, random-walk step size, and sphere aggregation. Modeled diffusion-rate reduction was found to be an approximately linear function of sphere-specific surface area (SSA), with no statistical differences observed between widely varying distributions having the same SSA. Incorporating consideration of diffusion capacity with the modeled diffusion-rate (tortuosity) effect and comparisons of resulting model predictions with limited, measured permeability data produced agreement with the measured permeability reduction effected by 100 phr of N660 in a bromobutyl polymer. Although more study and application is clearly needed, the model appears to be useful for estimating the path-tortuosity contribution to the decrease in permeability brought about by incorporation of solid, impermeable fillers in a permeable matrix.

REFERENCES

[1]W. M. Hess and C. R. Herd, "Microstructure, Morphology, and General Physical Properties," in *Carbon Black Science and Technology*, 2nd ed., J.-B. Donnet, R. C. Bansal, and M.-J. Wang, Eds., Marcel Dekker, Inc., New York, 1993, Ch. 3.

[2]G. J. van Amerongen, RUBBER CHEM. TECHNOL. **28**, 821 (1955).

[3]G. J. van Amerongen, RUBBER CHEM. TECHNOL. **37**, 1065 (1964).

[4]C. Nah and M. A. Kader, "Barrier Properties of Rubber Nanocomposites," *Rubber Nanocomposites: Preparation, Properties and Applications*, S. Thomas and R. Stephen, Eds., John Wiley and Sons, Asia, 2010, Ch. 18.

[5]R. R. Juengel, D. C. Novakoski, and S. G. Laube, "Effect of Carbon Black Loading, Surface Area and Polymer Type on the Permeability of Innerliner Compounds," International Tire Exhibition & Conference, 1994.

[6]D. Hardy, H. Moneypenny, M. Holderied, J. Harris, R. Campion, and G. Morgan, "Low Surface Area Carbon Black for Tire Innerliner," Paper 2, presented at the 156th Meeting of the Rubber Division, ACS, Antwerp, Belgium, November 22–23, 1999.

[7]B. Rodgers, R. N. Webb, and W. Weng, *Rubber World* **234**, 36 (2006).

[8]D. J. Lohse, *Rubber World* **240**, 36 (2009).

[*Paper 19, presented at the Fall 180th Technical Meeting of the Rubber Division, ACS (Cleveland, OH), 11–13 October 2011*]

[*Received September 2011, Revised May 2012*]

APPENDIX A: COMPUTATIONAL MODELING PROCESS

Execution of the modeling algorithm developed by the authors was performed in parallel on a network of many multiprocessor and/or multicore computers. For each data point, a distribution of spheres was built up randomly by selecting one sphere at a time from a log-normal distribution of a given mean and heterogeneity index (HI = [weight mean/mean]) until the prescribed loading was achieved. A rubber (matrix) density of 0.93 g/cm^3 and a carbon black (sphere) density of 1.86 g/cm^3 were assumed.

For nonaggregating spheres, once the distributions were populated, spheres were placed into a model compound sample volume from largest to smallest to expedite compound modeling at higher loadings. For spheres allowed to aggregate, the overlap of volume in intersecting spheres was adjusted for and calculated by adding additional spheres to achieve the prescribed loading. Accounting for the overlap between aggregated spheres in the loading calculations was handled by measuring the actual occupied volume on sphere insertion and counting the portions of space enclosed by more than one sphere only once. Transmission electron microscope (TEM) imaging shows that carbon black particles do overlap to an appreciable degree. Therefore, carbon blacks have slightly lower specific surface area (SSA) than would be present if the constituent spheres were completely separate (which occurs in significant quantities only in thermal carbon blacks). This is accounted for, in practice, by the specification and control of carbon-black fineness by SSA, not sphere size distribution. Aggregation of spheres in the current study reduces the available filler SSA to a small degree.

For each iteration, a cube of dimensions 20 times the mean sphere size per side was used for the sample volume (e.g., for a 50 nm MSS, a 1-μm cube was used). To place a sphere, random x, y, and z coordinates in the volume were chosen. In the nonaggregated models, if the sphere overlapped any previously placed sphere, it was removed and replaced in a new random location until it did not overlap any previously placed spheres. Periodic boundary conditions were used, meaning that each sample volume continued indefinitely in each direction (x, y, and z) with repeated sample volume cells. To simulate diffusion through these model compounds, a biased, random-walk method was employed on dimensionless particles. The direction of the bias vector was slightly offset from the sample volume cell z-axis so that the diffusing particle would tend to sample different parts of the cell on different passes through the modeled infinite periodic volume. The bias-vector magnitude was arbitrarily set to 1 nm; this vector is described by $\mathbf{B} = (1/7)\mathbf{i} + (1/9)\mathbf{j} + [1 - (1/7)^2 - (1/9)^2]^{0.5}\mathbf{k}$ nm. The direction of the step vector was selected by choosing a random azimuthal angle ϕ (angle from x-axis in x–y plane), and a random altitude angle (angle from x–y plane) having a probability weighted by cos θ, with 1° resolution in each angular coordinate. For each iteration, the diffusion vector was calculated as the sum of the step vector (random) and the bias vector (constant) ($\mathbf{D} = \mathbf{S} + \mathbf{B}$). This resulted in a random-walk biased parallel to $\mathbf{B}$, as follows: The diffusion vector was applied to the present particle location. If no intersections with sphere boundaries were detected for this

vector, the particle was stepped, a new random vector was constructed, and the process was repeated. Whenever the diffusion vector intersected a sphere boundary, specular reflection from the plane tangent to the sphere surface at the collision point was enacted, and the remainder of the diffusion vector was carried out by the particle in the new reflected direction (subject to subsequent collisions as well). Then a new random vector was constructed, and the process was repeated.

Diffusion was carried out for 50 μm, traveled parallel to **B**, for each volume, and the number of steps to reach that distance was counted. Because the magnitude of the bias vector was 1 nm, the ratio of the distance traveled parallel to **B** to the number of steps gives the modeled permeability as a percentage of the value in an unfilled volume.

The relationship between carbon black phr, weight fraction, and volume fraction must be kept in mind. (Note—for simplicity, rubber compound ingredients other than rubber and spherical fillers are ignored in this study.) A given increase in phr produces smaller increases in carbon-black weight fraction and volume fraction as loading is increased. As a point of reference, 100 phr carbon black is 50% weight-fraction carbon black, but only 33.3% volume-fraction carbon black, with weight and volume percentage differences being due to density differences between rubber and carbon black. As loadings are increased, progressively greater differences in phr carbon black may be needed to effect a given change in diffusion rate.

APPENDIX B: MODELING DATA TABLES

*Indicates algorithm stalled due to particle trapping in well.

TABLE B.I
AGGREGATED, HI = 1.5, 5-NM STEP VECTOR (DECREASE IN MODELED DIFFUSION RATE RELATIVE TO 0 PHR)

	20 phr, %	40 phr, %	60 phr, %	80 phr, %	100 phr, %
30 nm	3.6	7.7	11.7	13.7	16.8
50 nm	3.2	6.4	9.2	13.1	15.9
70 nm	3.1	6.2	8.9	12.4	*
100 nm	3.2	6.4	9.5	12.2	15.9
150 nm	2.5	6.3	9.3	*	*
200 nm	2.8	6.3	8.6	*	*
300 nm	2.6	4.5	*	*	*
500 nm	2.5	5.2	*	*	*

TABLE B.II
AGGREGATED, HI = 1.5, 10-NM RANDOM-WALK VECTOR (DECREASE IN MODELED DIFFUSION RATE RELATIVE TO 0 PHR)

	20 phr, %	40 phr, %	60 phr, %	80 phr, %	100 phr, %
30 nm	6.0	10.1	12.7	17.6	20.2
50 nm	3.8	8.2	12.1	14.3	17.2
70 nm	3.0	8.5	12.1	13.9	16.9
100 nm	3.9	7.9	10.3	13.6	16.0
150 nm	3.1	7.1	10.4	12.7	14.8
200 nm	2.9	7.4	9.5	12.5	14.8
300 nm	2.0	6.3	8.6	11.4	13.1
500 nm	2.1	6.3	*	*	*

TABLE B.III
AGGREGATED, HI = 1.5, 20-NM RANDOM-WALK VECTOR (DECREASE IN MODELED DIFFUSION RATE RELATIVE TO 0 PHR)

	20 phr, %	40 phr, %	60 phr, %	80 phr, %	100 phr, %
30 nm	6.1	13.3	19.6	22.1	26.9
50 nm	3.8	11.8	16.1	17.1	22.7
70 nm	5.9	11.6	13.4	17.4	19.5
100 nm	5.6	9.5	13.1	15.6	18.7
150 nm	3.7	8.1	12.1	14.6	18.3
200 nm	4.4	7.5	9.7	13.9	18.0
300 nm	2.9	7.4	11.0	12.8	15.7
500 nm	3.5	6.0	10.9	*	15.9

TABLE B.IV
AGGREGATED, HI = 2.5, 5-NM RANDOM-WALK VECTOR (DECREASE IN MODELED DIFFUSION RATE RELATIVE TO 0 PHR)

	20 phr, %	40 phr, %	60 phr, %	80 phr, %	100 phr, %
30 nm	2.9	7.0	9.8	12.8	15.9
50 nm	3.6	5.9	8.8	12.1	15.7
70 nm	3.3	6.1	8.9	11.0	14.2
100 nm	2.8	5.5	7.6	*	*
150 nm	2.7	*	8.5	*	*
200 nm	2.5	5.2	*	*	*
300 nm	2.6	*	8.2	*	*
500 nm	2.6	5.2	*	*	*

TABLE B.V
AGGREGATED, HI = 2.5, 10-NM RANDOM-WALK VECTOR (DECREASE IN MODELED DIFFUSION RATE RELATIVE TO 0 PHR)

	20 phr, %	40 phr, %	60 phr, %	80 phr, %	100 phr, %
30 nm	5.3	9.7	12.7	15.5	19.0
50 nm	4.3	7.5	10.6	14.4	16.9
70 nm	3.7	6.4	10.8	13.0	14.6
100 nm	3.1	5.9	9.9	12.8	16.1
150 nm	3.7	6.4	10.0	12.3	16.3
200 nm	2.6	6.9	8.7	11.1	14.5
300 nm	2.2	5.1	7.2	*	13.1
500 nm	3.4	5.9	7.4	*	*

TABLE B.VI
AGGREGATED, HI = 2.5, 20-NM RANDOM-WALK VECTOR (DECREASE IN MODELED DIFFUSION RATE RELATIVE TO 0 PHR)

	20 phr, %	40 phr, %	60 phr, %	80 phr, %	100 phr, %
30 nm	5.6	10.8	15.4	20.4	25.4
50 nm	10.8	10.1	15.1	16.5	21.7
70 nm	3.1	8.3	13.6	17.3	18.0
100 nm	4.4	8.7	12.2	15.1	19.6
150 nm	4.3	9.0	10.9	12.9	18.3
200 nm	4.5	7.8	10.7	13.4	16.2
300 nm	−0.5	6.2	10.7	13.2	11.9
500 nm	2.9	8.4	10.3	10.7	*

TABLE B.VII
NONAGGREGATED, HI = 1.5, 1-NM RANDOM-WALK VECTOR (DECREASE IN MODELED DIFFUSION RATE RELATIVE TO 0 PHR).

	20 phr, %	40 phr, %	60 phr, %	80 phr, %	100 phr, %
30 nm	2.4	4.6	6.1	7.7	9.2
50 nm	2.5	4.5	6.0	7.4	8.6
70 nm	2.6	4.2	6.0	7.4	8.7
100 nm	2.6	4.3	5.8	7.1	8.6
150 nm	2.4	4.2	5.7	7.3	8.5
200 nm	2.2	4.2	5.6	6.9	8.5
300 nm	2.6	4.0	5.9	7.3	8.2
500 nm	2.1	4.4	5.7	7.0	7.9

TABLE B.VIII
NONAGGREGATED, HI = 1.5, 2-NM RANDOM-WALK VECTOR (DECREASE IN MODELED DIFFUSION RATE RELATIVE TO 0 PHR).

	20 phr, %	40 phr, %	60 phr, %	80 phr, %	100 phr, %
30 nm	2.7	4.8	7.0	8.8	10.0
50 nm	2.4	4.5	6.4	8.3	9.3
70 nm	2.5	4.5	6.3	7.8	8.9
100 nm	2.6	4.4	6.2	7.6	8.7
150 nm	2.2	4.2	6.1	7.4	8.5
200 nm	2.2	4.4	6.1	7.2	8.3
300 nm	2.0	3.8	5.3	7.1	8.0
500 nm	2.2	4.1	5.4	6.6	8.6

TABLE B.IX
NONAGGREGATED, HI = 1.5, 5-NM RANDOM-WALK VECTOR (DECREASE IN MODELED DIFFUSION RATE RELATIVE TO 0 PHR).

	20 phr, %	40 phr, %	60 phr, %	80 phr, %	100 phr, %
30 nm	4.2	6.7	9.3	11.7	14.1
50 nm	2.8	5.2	8.3	10.2	12.3
70 nm	3.3	5.5	7.3	9.4	11.4
100 nm	2.9	5.3	7.4	8.9	10.2
150 nm	2.6	4.4	7.1	8.3	9.1
200 nm	2.9	5.2	7.1	7.6	9.2
300 nm	2.5	4.5	6.3	7.6	9.2
500 nm	2.4	4.2	5.5	7.0	9.1

TABLE B.X
NONAGGREGATED, HI = 1.5, 10-NM RANDOM-WALK VECTOR (DECREASE IN MODELED DIFFUSION RATE RELATIVE TO 0 PHR).

	20 phr, %	40 phr, %	60 phr, %	80 phr, %	100 phr, %
30 nm	4.3	9.5	12.6	14.9	19.1
50 nm	4.1	8.6	10.3	14.2	16.0
70 nm	4.6	6.6	10.5	13.0	15.1
100 nm	3.5	7.4	8.7	12.0	13.2
150 nm	3.7	5.5	9.0	9.2	11.9
200 nm	3.0	5.3	8.0	9.5	12.4
300 nm	2.4	5.5	6.9	9.2	11.0
500 nm	2.8	4.1	7.5	7.7	10.9

TABLE B.XI
NONAGGREGATED, HI = 1.5, 20-NM RANDOM-WALK VECTOR (DECREASE IN MODELED DIFFUSION RATE RELATIVE TO 0 PHR).

	20 phr, %	40 phr, %	60 phr, %	80 phr, %	100 phr, %
30 nm	6.2	13.2	17.6	22.6	24.9
50 nm	5.3	11.5	15.0	18.2	20.0
70 nm	6.2	10.0	13.0	14.6	18.5
100 nm	5.3	7.2	12.4	12.5	16.7
150 nm	6.0	7.3	9.0	13.3	14.8
200 nm	3.8	8.0	9.2	12.7	14.7
300 nm	4.1	5.2	9.6	12.2	11.4
500 nm	3.4	6.1	8.1	11.1	9.7

TABLE B.XII
NONAGGREGATED, HI = 2.5, 1-NM RANDOM-WALK VECTOR (DECREASE IN MODELED DIFFUSION RATE RELATIVE TO 0 PHR).

	20 phr, %	40 phr, %	60 phr, %	80 phr, %	100 phr, %
30 nm	2.5	4.6	6.2	7.9	9.0
50 nm	2.5	4.2	6.1	7.4	8.6
70 nm	2.4	4.6	6.0	7.2	8.7
100 nm	2.3	4.4	5.7	7.3	8.3
150 nm	2.0	4.8	5.4	7.5	8.2
200 nm	2.7	4.5	5.5	7.1	7.8
300 nm	2.7	4.1	5.4	6.6	8.0
500 nm	2.9	3.7	5.7	6.7	8.2

TABLE B.XIII
NONAGGREGATED, HI = 2.5, 2-NM RANDOM-WALK VECTOR (DECREASE IN MODELED DIFFUSION RATE RELATIVE TO 0 PHR).

	20 phr, %	40 phr, %	60 phr, %	80 phr, %	100 phr, %
30 nm	3.0	4.9	7.1	8.2	9.5
50 nm	2.5	4.6	6.4	7.9	9.3
70 nm	2.6	4.5	6.4	7.4	9.3
100 nm	2.7	4.8	5.7	7.6	8.6
150 nm	2.4	4.2	5.5	7.2	8.8
200 nm	2.3	3.9	5.6	7.0	7.7
300 nm	2.1	3.8	5.8	7.1	8.7
500 nm	2.0	3.4	6.2	8.0	8.3

TABLE B.XIV
NONAGGREGATED, HI = 2.5, 5-NM RANDOM-WALK VECTOR (DECREASE IN MODELED DIFFUSION RATE RELATIVE TO 0 PHR).

	20 phr, %	40 phr, %	60 phr, %	80 phr, %	100 phr, %
30 nm	3.3	6.5	8.4	10.7	13.0
50 nm	3.2	5.9	8.0	9.6	11.4
70 nm	2.9	5.1	7.0	9.4	10.6
100 nm	3.1	5.2	7.0	8.4	10.4
150 nm	2.4	5.1	6.6	7.5	9.4
200 nm	2.5	5.0	6.5	7.7	8.4
300 nm	2.3	4.5	6.0	7.7	9.4
500 nm	2.1	4.3	5.9	7.6	8.1

TABLE B.XV
NONAGGREGATED, HI = 2.5, 10-NM RANDOM-WALK VECTOR (DECREASE IN MODELED DIFFUSION RATE RELATIVE TO 0 PHR).

	20 phr, %	40 phr, %	60 phr, %	80 phr, %	100 phr, %
30 nm	4.7	8.6	11.3	13.9	17.1
50 nm	3.8	6.7	9.5	12.7	14.5
70 nm	3.7	5.9	9.3	11.9	13.3
100 nm	3.6	6.4	7.5	11.1	11.7
150 nm	2.7	6.3	7.7	10.0	12.6
200 nm	3.0	4.1	7.8	9.7	10.7
300 nm	3.6	5.0	7.2	8.4	10.7
500 nm	2.4	4.6	6.8	8.4	9.5

TABLE B.XVI
NONAGGREGATED, HI = 2.5, 20-NM RANDOM-WALK VECTOR (DECREASE IN MODELED DIFFUSION RATE RELATIVE TO 0 PHR).

	20 phr, %	40 phr, %	60 phr, %	80 phr, %	100 phr, %
30 nm	3.4	12.2	15.8	18.3	21.9
50 nm	7.2	9.5	12.7	15.4	18.8
70 nm	5.3	8.2	12.9	15.3	16.3
100 nm	4.5	8.7	10.8	13.3	15.4
150 nm	6.2	7.7	11.1	13.1	15.2
200 nm	2.7	8.2	8.3	12.1	12.3
300 nm	4.3	6.7	8.5	10.0	12.4
500 nm	3.6	4.3	9.3	10.6	12.4